Gas Permeability, Solubility, and Diffusion Coefficients in 1,2-Polybutadiene Containing Magnesium Oxide

Scott Matteucci,[†] Roy D. Raharjo,[†] Victor A. Kusuma,[†] Steve Swinnea,[‡] and Benny D. Freeman*[,†]

Department of Chemical Engineering, The University of Texas at Austin, 10100 Burnet Road, Building 133, Austin, Texas 78758l, and Texas Materials Institute, College of Engineering, The University of Texas at Austin, 1 University Station C2201, Austin, Texas 78712

Received November 6, 2007; Revised Manuscript Received January 7, 2008

ABSTRACT: Magnesium oxide nanoparticles (3 nm) were dispersed in 1,2-polybutadiene via solution casting. Particles were observed to be dispersed into submicron aggregates using atomic force microscopy and transmission electron microscopy. The nanocomposite density was consistently lower than that anticipated on the basis of an additive model, suggesting the presence of voids in the nanocomposites. The incorporation of nanoparticles into 1,2-polybutadiene increased acid gas (i.e., CO_2) and nonpolar gas (i.e., CH_4, N_2) permeability with increasing particle loading. For instance, CO_2 permeability increased from 52 barrer in the unfilled polymer to 650 barrer in a nanocomposite containing 27 vol % (nominal) MgO, at 35 °C and a feed pressure of 12 atm. CO_2/nonpolar gas selectivity decreased with increasing particle loading, while CH_4/N_2 selectivity was not influenced by the particles. Gas solubility increased systematically with increasing particle loading. In contrast, gas diffusion coefficients initially decreased with increasing particle loading and then increased with increasing loading at particle loadings greater than 10 vol % (nominal).

Introduction

Polymeric membranes are currently used for CO_2/CH_4 separations,[1] and certain materials have been considered for use to remove CO_2 from flue gases.[1,2] Typically, a “tradeoff” relationship between permeability and selectivity exists, with materials having higher permeability having lower selectivity, and vice versa.[3,4] This upper bound has been related to gas molecule size and condensability.[3,4] Changing polymer chemical structure alone rarely yields materials that exceed the upper bound in polymeric materials.[5,6] In attempts to circumvent the limitations imposed by the permeability/selectivity tradeoff in polymers, inorganic particles have been dispersed in polymers as one potential route to modify gas diffusion and/or solubility in ways that cannot be achieved using polymers alone.[7−12] For example, O_2/N_2 selectivity increased from 3.7 in poly(ether sulfone) to 4.4 when 50 wt % zeolite 4A was added.[7] In another study, fumed silica or TiO_2 nanoparticles dispersed in some disubstituted polyacetylenes increased both gas permeability and selectivity.[8−11]

Impermeable particles that interact with penetrant gases have been dispersed in polymers to modify selectivity.[13,14] For example, propane/propylene mixed gas selectivity increased from ∼1 in poly(ethylene-*co*-propylene) to ∼180 in a film containing 50 wt % silver nanoparticles treated with *p*-benzoquinone.[14] Other groups have used CO_2-sorbing nanoparticles to increase CO_2 solubility in nanocomposite films.[15,16]

This study describes the incorporation of magnesium oxide nanoparticles in 1,2-polybutadiene. The nanoparticles have a high surface area (i.e., greater than 600 m^2/g) and are basic, so they physisorb CO_2.[17,18] These nanoparticles can adsorb large concentrations of CO_2 even at low pressures.[20] Gas permeability and acid gas/nonpolar gas selectivity in nanocomposite films are reported for pure and mixed gas feed streams. The influence of the particles on gas permeability is discussed in terms of the effects of the particles on gas solubility and gas diffusivity. Particle dispersion is characterized by atomic force microscopy and transmission electron microscopy.

Background

Gas Transport Theory. P_A, the steady-state permeability of gas A in a polymer, is defined as follows:[5]

$$P_A \equiv \frac{N_A l}{p_2 - p_1} \tag{1}$$

where N_A is the steady-state flux of A through the film, l is the film thickness, and p_2 and p_1 are the feed and permeate partial pressures of gas A, respectively. If the gas does not obey the ideal gas law, the partial pressures in this equation are replaced by fugacities.[19] When the downstream pressure is much lower than the upstream pressure and Fick’s law governs the diffusion of gas through the polymer, permeability can be expressed as[5]

$$P_A = D_A S_A \tag{2}$$

where D_A is the effective concentration-averaged diffusion coefficient of gas A. The solubility coefficient of gas A in the polymer, S_A, is defined as[5]

$$S_A = C/p_2 \tag{3}$$

where C is the concentration of gas sorbed in the polymer at the upstream surface.[5]

The ideal selectivity, $\alpha_{A/B}$, characterizes the ability of a polymer to separate two gases, A and B:[5]

$$\alpha_{A/B} \equiv \frac{P_A}{P_B} \tag{4}$$

---

* Corresponding author: Tel +01-512-232-2803, Fax +01-512-232-2807, e-mail freeman@che.utexas.edu.

[†] Department of Chemical Engineering,.

[‡] Texas Materials Institute, College of Engineering.

10.1021/ma702459k CCC: $40.75

Substituting eq 2 into eq 4 provides the following relationship:

$$\alpha_{A/B} = \frac{D_A}{D_B}\frac{S_A}{S_B} \tag{5}$$

Diffusivity selectivity, D_A/D_B, depends primarily on the polymer size-sieving capability (i.e., the ability for a polymer to separate gas molecules of different sizes), polymer free volume, and the size of the penetrant gases.[5] The size-sieving behavior of a polymer is dependent on a number of parameters such as polymer chain mobility and polymer structure.[5] Solubility selectivity, S_A/S_B, depends mainly on the condensability of the penetrants gases and the affinity between the gases and the polymer matrix.[5]

Modeling Permeability in Heterogeneous Materials. Bruggeman's model has been used to describe permeability over a wide range of dispersed phase concentrations in polymer composite systems.[20−22] This model has two limits. The upper limit of the permeability of a composite, P_C, predicted by the model is obtained when the dispersed phase permeability, P_D, is much greater than that of the matrix, P_M:[20]

$$\frac{P_C}{P_M} = \frac{1}{(1-\phi_D)^3} \tag{6}$$

where ϕ_D is the volume fraction of the dispersed phase. At the other extreme, if the dispersed phase permeability is much less than that of the matrix, then the resulting permeability of a composite is given by[20]

$$\frac{P_C}{P_M} = (1-\phi_D)^{3/2} \tag{7}$$

Materials and Methods

Spherical periclase (i.e., MgO) nanoparticles (Nanoscale, Manhattan, KS) were used in this study. The particles have a density of 3.58 g/cm^3 according to the supplier. The BET surface area was between 600 and 640 m^2/g, which corresponds to an equivalent spherical particle diameter of $<\sim$3 nm. The particles were reported by the manufacturer to be >95% magnesium, based on metal. The 1,2-polybutadiene (PB) (Scientific Polymer Products, Inc., Ontario, NY) has an approximate molecular weight of 100 000 g/mol; it had 7% cis and 93% vinyl structure. CH_4, CO_2, and N_2 were obtained from Airgas (Radnor, PA), and all gases were at least 99% pure. The CO_2/CH_4 gas mixtures used in this study were from Air Liquide (Houston, TX). The test gases, PB, and MgO nanoparticles were used as received.

All sample preparation was conducted in a glovebox under a N_2 blanket. 1.5 g of 1,2-polybutadiene was dissolved in 20 mL of dry toluene (i.e., toluene containing no more than 50 ppm water (Acros Organics, Geel, Belgium)) and stirred at 40 °C for 1 h, which was sufficient for the polymer to completely dissolve. The nanoparticles, which deaggregate readily in common organic solvents such as toluene,[23] were added to the solution in an amount that would result in a final dry film with a predetermined nominal volume fraction of particles, ϕ_F^N:[11]

$$\phi_F^N = \frac{M_F/\rho_F}{M_P/\rho_P + M_F/\rho_F} \tag{8}$$

where M_F and M_P are the masses of particles and polymer in the sample, respectively. ρ_F and ρ_P are the pure component density values of the particles and polymer, respectively. The particle-filled solution was allowed to mix for 20 min at 40 °C using a magnetic stir bar. The solution was poured onto a level glass casting plate, and the solvent was allowed to completely evaporate over a period of 24 h.

Polymer and nanocomposite cross sections for atomic force microscopy (AFM) were prepared using cryoultramicrotomy. Samples were processed, using a razor blade, into sizes that could be mounted on a microtome. 1,2-Polybutadiene and nanocomposite samples were polished at −100 °C, which was significantly lower than the T_g of 1,2-polybutadiene (i.e., −19 to −9 °C),[24] using a RMC-Boeckeler PowerTome PT-XL (Boeckeler Instruments Inc., Tucson, AZ) equipped with a cryo diamond knife from Micro Star Technologies (Huntsville, TX) at a cutting speed of 0.6 mm/s.

1 μm by 1 μm nanocomposite AFM tapping mode phase profiles were acquired using a Digital Instruments Dimension 3100 with Nanoscope IV controller (Woodbury, NY) using silicon NCH AFM tips from Nanoworld (Neuchatel, Switzerland). These phase profiles were used to characterize particle dispersion and aggregate size in film cross sections. Samples were scanned at 0.8 Hz. Each image contained 512 lines. The resolution was 2 nm per line.

All subsequent image analysis utilized ImageJ software from the National Institutes of Health, using a protocol discussed elsewhere.[11] The aggregate area distribution, as determined by ImageJ analysis, was divided into 100 bins of equal area increments. The area increment for one bin was 1.4 nm^2 for films containing 10 and 13 vol % (nominal) MgO. The nanoparticle aggregate diameter results were not significantly influenced by the number of bins used as long as at least 50 bins were used in the data analysis. The aggregates were approximated as spheres, so the area of the nanoparticle aggregates in bin j, A_j, was converted to an effective aggregate diameter, d_j, as follows:[11]

$$d_j = \sqrt{\frac{4A_j}{\pi}} \tag{9}$$

The fraction of aggregates with a diameter of d_j, F_j, is[11]

$$F_j = \frac{N_j}{N_T} \tag{10}$$

where N_j is the number of distinguishable nanoparticle aggregates of diameter d_j. N_T is the sum of N_j over all d_j, and its value depended upon particle loading. The aggregate diameters were fit to a Weibull distribution, which is an empirical model often used to characterize particle size distributions:[25−28]

$$F_j = \frac{\beta}{\alpha}\left(\frac{d_j-\upsilon}{\alpha}\right)^{\beta-1}\exp\left[-\left(\frac{d_j-\upsilon}{\alpha}\right)^{\beta}\right] \tag{11}$$

where β and α are fitting parameters and υ is the diameter of the nanoparticles (i.e., the smallest possible value of d_j). In this equation, d_j must be $\geq \upsilon$.

The average aggregate diameter, $\bar{d}$, was calculated as follows:[27]

$$\bar{d} = \frac{1}{N_T}\sum_{j=1}^{m} d_j N_j \tag{12}$$

where m is the number of bins (i.e., 100) used in this study. The standard deviation in the average aggregate diameter, σ, is[27]

$$\sigma = \left(\frac{1}{N_T}\sum_{h=1}^{m}[(d_h-\bar{d})^2 N_h]\right)^{1/2} \tag{13}$$

Transmission electron microscopy (TEM) samples were trimmed using a razor blade in a manner similar to that used for AFM sample preparation. The samples were embedded in LR White resin (Electron Microscopy Sciences, Hatfield, PA) and were pretrimmed using a glass knife at room temperature with a Leica Ultracut UCT microtome (Leica Microsystems GmbH, Wetzlar, Hesse, Germany) to form small, pyramidal shapes containing an exposed sample surface with a smooth rectangular face $\sim$100−200 μm in length and width. Sample sections that were $\sim$50 nm thick were removed

Table 1. Concentration of Crystalline 1,2-Polybutadiene and Polymer/Nanocomposite Glass Transition Temperature[a]

ϕ_F^N (%)	technique for estimating crystallinity	χ_C (%)	ϕ_C (%)	$T_g{}^c$ (°C)
0	density[b]	30 ± 5	28 ± 4	
0	DSC	35 ± 3	33 ± 3	−17 ± 3
0	WAXD	32 ± 3	30 ± 3	
10	WAXD	22 ± 2	20 ± 2	−10 ± 3
20	WAXD	16 ± 2	15 ± 2	−9 ± 3
27	WAXD	15 ± 2	14 ± 2	−8 ± 3

[a] Uncertainties were estimated using the propagation of errors method.[25] [b] χ_C values were estimate from density using eq 20; ϕ_C values for DSC and WAXD were estimated using eq 20. [c] All T_g values were determined from first scan DSC thermograms.

from the pyramid using a cryo diamond knife operating at −100 °C and at a cutting speed of 0.6 mm/s. These sections were floated on a 60/40 mixture of DMSO/water in a diamond knife boat at −60 °C, from which they were scooped onto 400-mesh copper TEM grids (Ted Pella Inc.). A FEI TECNAI G^2 F20 TEM (FEI Co., Hillsboro, OR) microscope was used at room temperature and an accelerating voltage of 200 kV.

A hydrostatic weighing method, employing a Mettler Toledo balance and a density determination kit, was used to determine PB and nanocomposite densities.[29] Deionized water (18.2 MΩ·cm prepared by a Milli-Q plus TOC, Millipore, Billerica, MA) served as the liquid phase in these experiments.

The polymer crystallinity, ϕ_C (volume of crystal/volume of polymer) was estimated from experimentally determined density values, as follows:[29]

$$\phi_C = \frac{\rho_P - \rho_A}{\rho_C - \rho_A} \tag{14}$$

where ρ_A and ρ_C are the densities of amorphous (i.e., 0.889 g/cm^3)[24] and crystalline (i.e., 0.963 g/cm^3)[30] PB, respectively. The measured density of the PB used in this study, ρ_P, was 0.911 ± 0.05 g/cm^3. The resulting crystallinity value is reported in Table 1 and will be discussed below.

As discussed elsewhere,[31] a Scintag $\theta-\theta$ diffractometer equipped with a Cu source and a solid-state detector was used to collect wide-angle X-ray powder diffraction (WAXD) patterns from ~3 cm^2 samples of each composite film. In order to compare nanoparticle mineral structures to known diffraction patterns, data were processed using the Jade version 7.5 (Materials Data Inc.) diffraction pattern processing software. To determine crystalline polymer concentration, backgrounds were modeled and removed from each diffraction pattern in a manner consistent with the literature.[32,33] An amorphous peak centered at about 14.5° 2θ was modeled for height, location, full width half-maximum (fwhm), and skew. Additionally, crystalline diffraction peaks for 1,2-polybutadiene were modeled for height, location, and fwhm. The weight fraction of crystalline material in the polymer phase, χ_C (grams of crystals/grams of polymer), was estimated as follows:[34]

$$\chi_C = \frac{I_C}{I_C + I_A} \tag{15}$$

where I_A and I_C are the integrated areas under the amorphous and crystalline peaks, respectively.

A Q-100 differential scanning calorimeter (DSC) from TA Instruments (New Castle, DE) was used to determine the glass transition temperature, T_g, of pure PB and the MgO filled nanocomposites and the crystallinity content of the unfilled polymer. The samples weighed between 10 and 20 mg. The DSC was programmed to lower the sample temperature from ambient to −80 °C at 20 °C/min. After holding the sample at −80 °C for 5 min, it was heated at 20 °C/min to 150 °C. The results from the initial heating sweep were used to determine the T_g values for all samples considered in this study. χ_C was calculated from the DSC thermogram of unfilled PB by comparing the polymer enthalpy of melting, ΔH_m, to the pure crystalline polymer enthalpy of melting, ΔH_C (i.e., 60.7 J/g),[24] as follows:[12]

$$\chi_C = \frac{\Delta H_m}{\Delta H_C} \tag{16}$$

While the DSC data could be used to determine the enthalpy of melting of the crystallites in the pure polymer, they could not be used for such determinations in the nanocomposite samples. In the DSC thermograms of the nanocomposite samples, there was a broad exotherm beginning at ~60 °C and extending, in some cases, to ~140 °C. This exotherm completely masked the melting endotherm of the polymer crystals, which, as indicated above, was observed between about 50 and 115 °C. The pure particles exhibit a broad endotherm beginning at temperatures above about 100 °C, which may be due to desorption of sorbed atmospheric gases. Thus, the exotherm in the nanocomposite samples did not correspond to any thermal event in either the pure polymer or the particles, suggesting that there could be an interaction or reaction of the particles with the polymer. PB is known to be sensitive to oxidative degradation that can be markedly accelerated in the presence of appropriate catalysts.[35,36] Metal oxides, such as MgO and ZnO, are known to vulcanize polybutadiene.[37,38] For these reasons, it was not possible to evaluate crystallinity in the nanocomposite samples from the DSC data.

CO_2, CH_4, and N_2 solubilities in neat 1,2-polybutadiene and MgO-filled nanocomposites were determined using a high-pressure barometric sorption apparatus.[39,40] The sorption chamber and sample films were degassed under vacuum for at least 18 h prior to conducting the experiments. Test gas pressure was increased at pressure intervals of between 3 and 5 atm from 2 to ~20 atm at 35 °C.

A constant volume/variable pressure apparatus[39,41] was used to determine pure gas permeability. Once a film was secured in the permeation cell, the film was degassed by exposing the upstream and downstream surfaces to vacuum overnight (i.e., at least 18 h). After degassing, the downstream volume was sealed at vacuum (i.e., pressure in the downstream volume was less than 1 × 10^{-4} atm), and the upstream volume was pressurized with a pure test gas. Gas permeability (cm^3 (STP) cm/(cm^2 s cmHg)) was calculated from the steady-state rate of pressure increase in the downstream volume as follows:

$$P = \frac{dp}{dt}\frac{lV}{TpAR} \tag{17}$$

where l is the film thickness (cm), dp/dt is the downstream volume steady-state pressure change (cmHg/s), p is the upstream absolute pressure (cmHg), T is experimental absolute temperature (K), A is the film area (cm^2), and V is the downstream volume (cm^3). R is the gas constant. Permeation experiments were conducted with a downstream pressure below 0.01 atm. The permeability values in this study are reported in units of barrer, which are

$$1 \text{ barrer} = 10^{-10} \frac{\text{cm}^3 \text{ (STP) cm}}{\text{cm}^2 \text{ s cmHg}} \tag{18}$$

The CO_2 and CH_4 mixed gas permeabilities were determined using a constant pressure/variable volume apparatus[42,43] equipped with a mass flow controller (MKS Instruments, Inc., Wilmington, MA) on the upstream side to regulate the residue flow rate. Helium was used to sweep the downstream side of the membrane and carry the permeate (i.e., CO_2 and CH_4) to a gas chromatograph. The total flow rate on the downstream side (i.e., helium plus permeate) was measured with a soap film flowmeter. The system temperature was controlled to ±0.1 °C using a constant temperature water bath.

The fugacity of the feed gas mixture was varied by changing the total upstream pressure and the feed gas composition. The feed gas compositions considered contained 20, 50, and 80 mol % CO_2, and the balance was CH_4. A sufficient residue flow rate at the upstream side was maintained to prevent concentration polarization

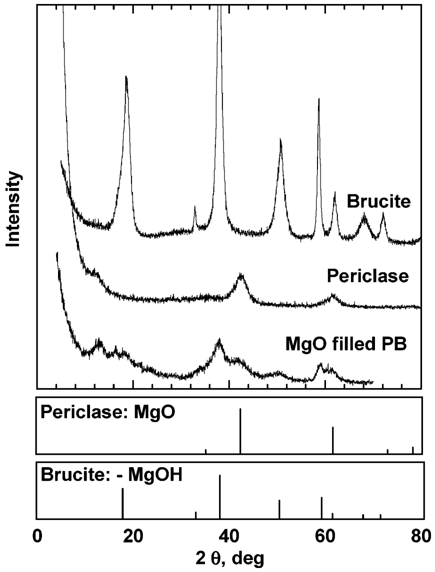

Figure 1. WAXD spectra of neat MgO nanoparticles that were exposed to ambient conditions for 1 week prior to testing (periclase),[31] MgO particles that were soaked in deionized water for 48 h and then dried for 48 h in a fume hood (brucite),[31] and a nanocomposite sample containing 20 vol % (nominal) MgO in 1,2-polybutadiene after 1 day of mixing at 40 °C (MgO filled PB). The boxes below the figure present 2θ peak locations and intensities associated with crystal structures of periclase and brucite from the powder diffraction database, PDF-2 Release 2004 from the International Centre for Diffraction Data, Newton Square, PA.

(i.e., a stage cut of less than 1%). The feed pressure was varied from 4.5 to 14.6 atm. The partial pressure of penetrants on the downstream side of the film being tested was maintained at or near zero (<0.05 atm) by adjusting the helium flow rate.

The steady-state gas permeability coefficient for each component in the mixture was calculated as follows:[44]

$$P_A = \frac{l}{f_{A,2} - f_{A,1}} \frac{273}{TA} \frac{p_{atm}}{76}\left(y_{A,1}\frac{dV}{dt}\right) \tag{19}$$

where $f_{A,2}$ and $f_{A,1}$ are the fugacities of gas A (cmHg) in the upstream and downstream, respectively. Measured partial pressure data were converted to fugacity values using the Soave–Redlich–Kwong (SRK) equation of state.[44] $y_{A,1}$ is the downstream mole fraction of gas A, p_{atm} is atmospheric pressure (cmHg), and dV/dt is the volumetric displacement rate of the soap film in the bubble flowmeter at steady state (cm^3/s). The coefficient 273/76 corrects the measured permeate gas flow rate to cm^3 (STP).

Results and Discussion

Nanoparticle Reactivity. Periclase (i.e., MgO) nanoparticles can react with water to form brucite (i.e., MgOH).[18,31] To determine whether this reaction occurred in the samples considered in this study, wide-angle X-ray diffraction spectroscopy was used to characterize the as-received particles, particles that had been soaked in water, and PB-based nanocomposite samples. The WAXD spectra from these studies are presented in Figures 1 and 2. As explained in more detail below, the location of the amorphous and crystalline peaks in the PB sample presented these figures is consistent with the literature.[24] On the basis of the results in Figure 1, the nanoparticles soaked in water exhibit a rather complete conversion from periclase to brucite. Even when precautions were taken to limit exposure of the samples to water during preparation, some of the nanoparticles in the PB-based nanocomposites also convert to brucite. Figure 2 shows that this reaction takes place in nanocomposites over the range of particle loadings used in this study. However, in contrast to previous studies, in which MgO particles were shown to react with a substituted acetylene polymer,[37] no evidence of reaction of the particles with PB was observed in FTIR studies.

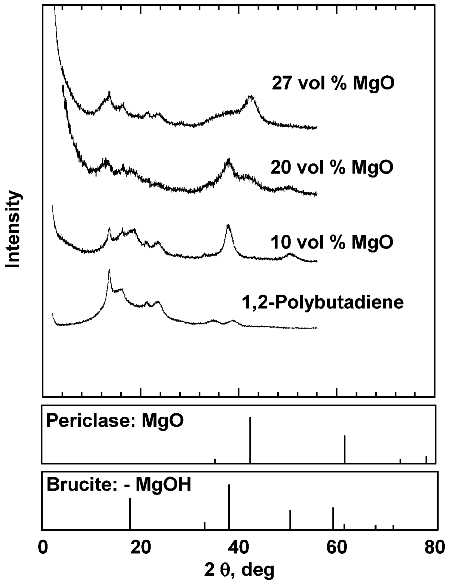

Figure 2. WAXD spectra of 1,2-polybutadiene and nanocomposites containing 10, 20, and 27 vol % (nominal) MgO in 1,2-polybutadiene after 1 day of mixing at 40 °C. The boxes below the graph present 2θ peak locations and intensities associated with crystal structures from the powder diffraction database, PDF-2 Release 2004 from the International Centre for Diffraction Data, Newton Square, PA.

Crystallinity and Glass Transition Temperature in PB and Nanocomposite Samples. Figure 2 presents the WAXD spectra for PB and PB–MgO nanocomposites. In unfilled PB, peaks are located at 13.2°, 16.0°, 21.6°, 24.0°, 35.0°, and 39.1° (2θ). The peak locations are consistent with literature values for PB containing 32 wt % crystallinity.[24] Generally, the peaks in the unfilled polymer were also observed in the PB–MgO nanocomposites. However, some of the PB peaks appear near or are overlapped by peaks attributed to either brucite or periclase. The peak located at ~13.2° (2θ) in the unfilled polymer shifts to higher 2θ values as particle loading increases in the nanocomposites. A similar shift has been reported for unfilled PB samples as crystal content decreases.[24] As will be discussed below, the concentration of crystalline PB decreases as particle content increases, so the peak shift at 13.2° (2θ) to higher 2θ values as particle loading increases agrees with the reduction in crystallinity observed at high particle concentrations.

Based on the WAXD data in Figures 1 and 2, the weight fraction of crystalline polymer in the polymer phase decreases as particle loading increases. The crystallinity values are presented in Table 1.[25] This trend is qualitatively consistent with that of PB filled with TiO_2 nanoparticles, where the weight fraction of crystals decreased from 32% in the unfilled polymer to 20% in samples containing 27 vol % (nominal) TiO_2.[12] The volume fraction of crystalline polymer in the polymer phase, ϕ_C (i.e., volume of crystalline polymer per total volume of polymer), was estimated as follows:[34]

$$\phi_C = \chi_C \frac{\rho_P^N}{\rho_C} \tag{20}$$

where ρ_P^N is the polymer density in the nanocomposite samples, which was calculated using the following equation:[24]

$$\frac{1}{\rho_{\rm P}^{\rm N}} = \frac{\chi_{\rm C}}{\rho_{\rm C}} + \frac{\chi_{\rm C} - 1}{\rho_{\rm A}} \qquad (21)$$

The crystalline volume fraction values, which are presented in Table 1, are useful in estimating the contribution of the polymer to the nanocomposite density, which is discussed below.

DSC thermograms of PB and representative nanocomposite samples are presented in Figure 3. The nanocomposite T_g increased with increasing particle loading, and the values obtained from the DSC results are recorded in Table 1. The T_g of the unfilled polymer is ~9 °C lower than that of the PB containing 27 vol % (nominal) MgO. Such behavior has been observed in other nanocomposites.[12,45] In the literature, such a shift in T_g is attributed to the adsorption of polymer onto the particle surface, which reduces the chain mobility of the bulk polymer.[45,46]

Nanoparticle Dispersion. Particle distribution in polymer matrixes can influence gas transport properties.[33,47,48] Traditionally, transmission electron microscopy (TEM) has been used to image particle dispersion in nanocomposites.[47,49] However, the nanoparticles used in such experiments generally had primary particle diameters greater than 10 nm, and such nanoparticles could be imaged using TEM without damaging the polymer phase.[33,47,48] Resolving individual nanoparticles with primary particle diameters below 5 nm often requires the TEM electron beam to be so focused that the polymer could be degraded upon even short exposure to the beam. Also, TEM samples are generally at least 40 nm thick. Since sample thickness could be many times the average interparticle spacing, as discussed below. Therefore, a 2-dimensional image of a 3-dimensional dispersion would show nanoparticles and nanoparticle aggregates overlapping even if the particles were well dispersed. Such overlap could cause errors in the determination of particle aggregate size from TEM images.

Tapping mode atomic force microscopy (AFM) provides images of the nanoparticle cross sections (i.e., nanocomposite bulk) with sufficient resolution to observe individually dispersed particles and small nanoparticle aggregates.[11] Figure 4 presents AFM tapping mode phase profile images for PB and nanocomposite cross sections. The unfilled PB (cf. Figure 4a) has two distinct phases that are attributed to amorphous and crystalline regions of the polymer.[12] The harder phase (i.e., white regions) in Figure 4a occupies ~27 area % of the AFM image, which is in good agreement with the volume percent of crystalline polymer as determined by density (28 ± 4 vol %), WAXD (30 ± 3 vol %), and DSC (34 ± 3 vol %). Therefore, the hard phase in unfilled PB is attributed to crystalline polymer.

Nanocomposite AFM images (i.e., Figure 4b,c) also contain two distinct phases. AFM phase profile images resolve the relative hardness of the surface being probed. The nanoparticles may be sufficiently hard that the modulus difference between crystalline and amorphous polymer cannot readily be resolved in the presence of particles, and such behavior has been reported.[12,50] Depending on the polymer and particle, AFM phase profile images have yielded mixed results for resolving amorphous polymer, crystalline polymer, and nanoparticles in such systems.[50−52]

Nearly 16 and 18 area % of the images in parts b and c of Figure 4, respectively, are occupied by the hard phase, which is in the same order as the particle concentration in the composites (i.e., 10 and 20 vol % (nominal) MgO, respectively). However, the area fraction of the hard phase in these AFM images (i.e., Figure 4b,c) is higher than concentration of crystalline polymer in the nanocomposite samples; the crystalline contents of the nanocomposite samples are recorded in Table 1. Therefore, the hard phase in the phase profiles is attributed solely to the nanoparticles.

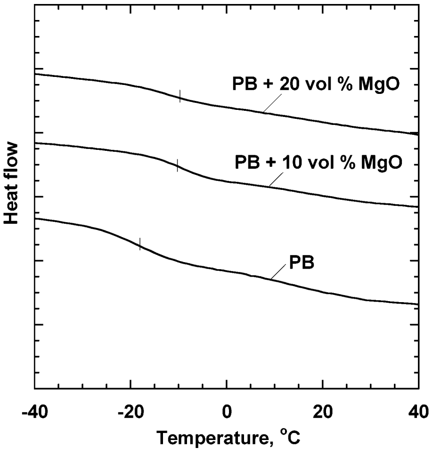

Figure 3. Influence of nominal volume percent MgO on the T_g of 1,2-polybutadiene filled with MgO nanoparticles. The T_g is recorded as the middle of the endothermic heat capacity step change in the DSC thermograms, which are represented by tick marks. All T_g values are from first run DSC scans. The thermograms have been displaced vertically for easier viewing.

Figure 5 presents the estimated characteristic particle diameter distribution for the nanoparticles and nanoparticle aggregates in Figure 4b,c and compares them to the best fit of a Weibull distribution to the data (i.e., eq 11).[25−27] A spherical model is used in calculating the aggregate diameters. The average aggregate diameter, $\bar{d}$, was estimated from the Weibull distribution as follows:[27]

$$\bar{d} = \sum_{j=1}^{h} d_j F_j \qquad (22)$$

where h is the number of bins used in the AFM particle analysis, (i.e., 100). The nanoparticle aggregates in Figure 4b,c have an average characteristic diameter $\bar{d}$ determined from the Weibull distribution of 7 ± 6 and 7 ± 3 nm, respectively. These results are consistent with the $\bar{d}$ calculated by eq 12, where the average particle diameter is 11 ± 6 and 8 ± 4 nm for PB films containing 10 and 13 vol % (nominal) MgO, respectively. Since the smallest structures the AFM can resolve (i.e., 2 nm) are similar to the nanoparticle diameter, a significant population of particles may not be resolved in these experiments, which would cause the experimentally derived $\bar{d}$ to be larger than the true average particle diameter in the nanocomposite.

Interaggregate spacing, d_a, can be estimated by assuming that the aggregates are spherical and dispersed in a body-centered-cubic structure:

$$d_{\rm a} = \bar{d}\left[\left(\frac{\pi}{6\phi_{\rm F}^{\rm N}}\right)^{1/3} - 1\right] \qquad (23)$$

d_a does not change significantly when either nominal or true volume fraction MgO (i.e., the particle concentration that accounts for any void volume in the nanocomposite)[11] is used in eq 23. A discussion regarding the differences between true and nominal volume fraction MgO in nanocomposites is provided below. The assumption of a body-centered-cubic aggregate structure is made solely to simplify estimating d_a. However, more realistic particle distributions (e.g., a random aggregate distribution)[53] yield very similar values for d_a. For the PB film containing 10 vol % (nominal) MgO, d_a is ~8 nm,

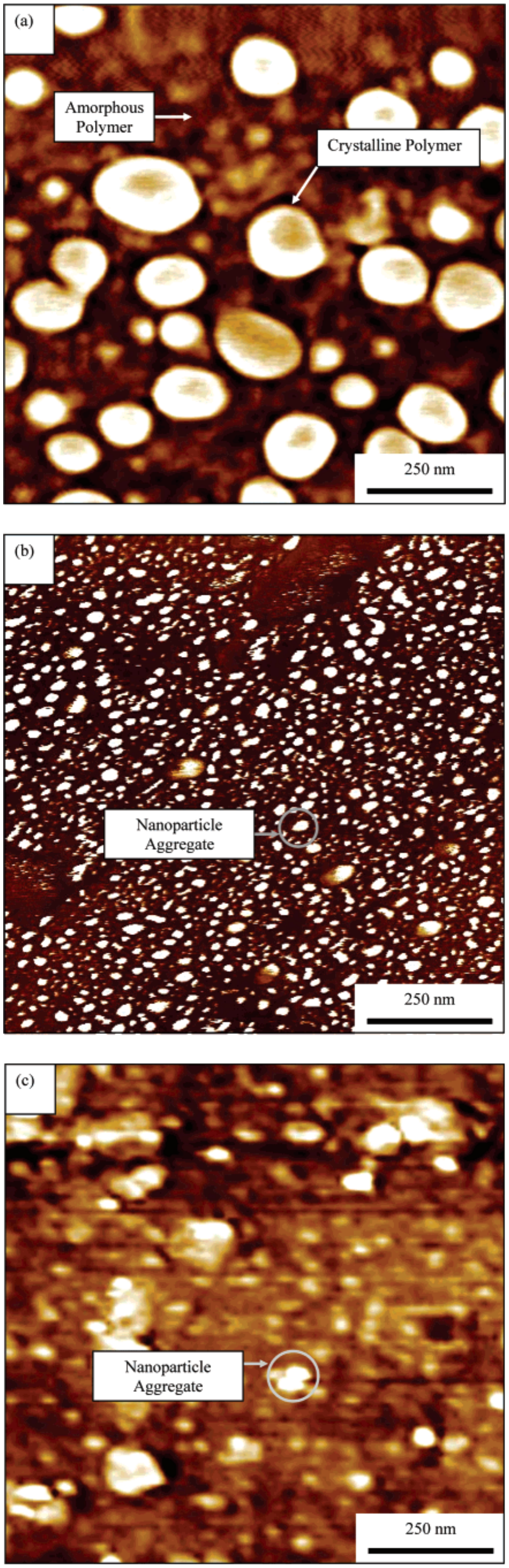

Figure 4. Tapping mode AFM phase profiles over a 1 μm by 1 μm region of (a) PB, (b) PB containing 10 vol % (nominal) MgO, and (c) PB containing 13 vol % (nominal) MgO. Hard phases are white.

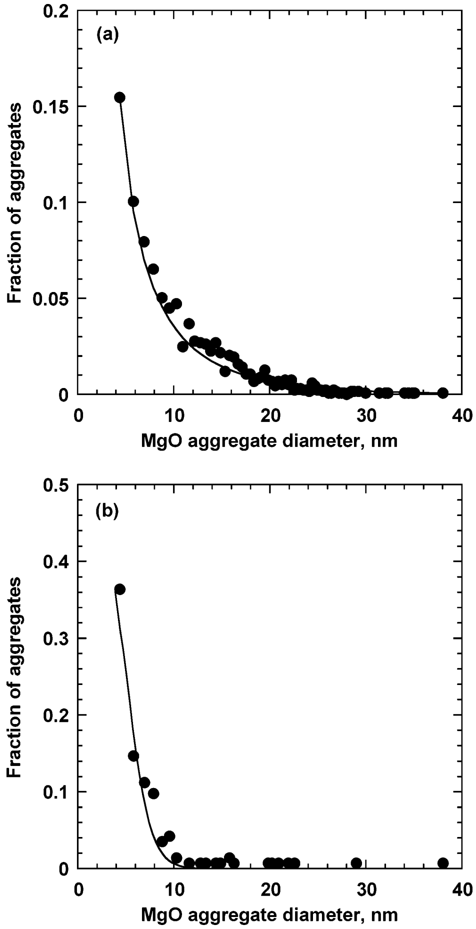

Figure 5. MgO aggregate diameter distribution from tapping mode phase profiles of PB containing (a) 10 vol % (nominal) MgO and (b) 13 vol % (nominal) MgO. The solid line represents a Weibull distribution with parameters of $\upsilon = 3.0$ nm, $\beta = 1.92 \pm 0.66$, and $\alpha = 0.75 \pm 0.32$ for plot (a) and $\upsilon = 3.0$ nm, $\beta = 2.57 \pm 0.83$, and $\alpha = 1.32 \pm 0.50$.[26,27] The error in the Weibull distribution parameters was determined by the least-squares fit method described by Bevington.[25]

Table 2. Nanoparticle Average Aggregate Diameter and Estimated Interparticle Spacing in Various Nanocomposites[11,12]

polymer	particle	$\phi_F^N \times$ 100 (%)	$\bar{d}$ (nm)	d_a (nm)	area % nanoparticles
PTMSP[13]	TiO_2[a]	3	7 ± 3	9	4
PTMSP[13]	TiO_2	10	12 ± 8	11	16
PB[14]	TiO_2	10	9 ± 4	7	6
PB	MgO	10	11 ± 6	8	16
PB	MgO	13	8 ± 4	4	18

[a] TiO_2 nanoparticles were ~3 nm in primary particle diameter.[11,12]

and d_a is 4 nm for PB films containing 13 vol % (nominal) MgO. These values are comparable to the estimated interaggregate distances reported in the literature for similar systems, as shown in Table 2.[11,12] Interparticle spacing in these nanocomposites are quite small even at moderate particle loadings. These interparticle spacings are comparable in magnitude to the structural features of PB molecules; for example, the radius of gyration of 1,2-polybutadiene used in this study is 8.5 nm.[12,54] One might anticipate that particles dispersed throughout the particle matrix at such short interparticle spacings should influence polymer chain packing, chain mobility, and gas transport properties.

Although TEM cannot resolve individual nanoparticles, it can characterize micron size nanoparticle aggregates. Figure 6 presents the TEM images for samples containing 10 and 20 vol % (nominal) MgO. The dark regions are electron rich (i.e., particle rich), and the lighter colored regions are electron poor

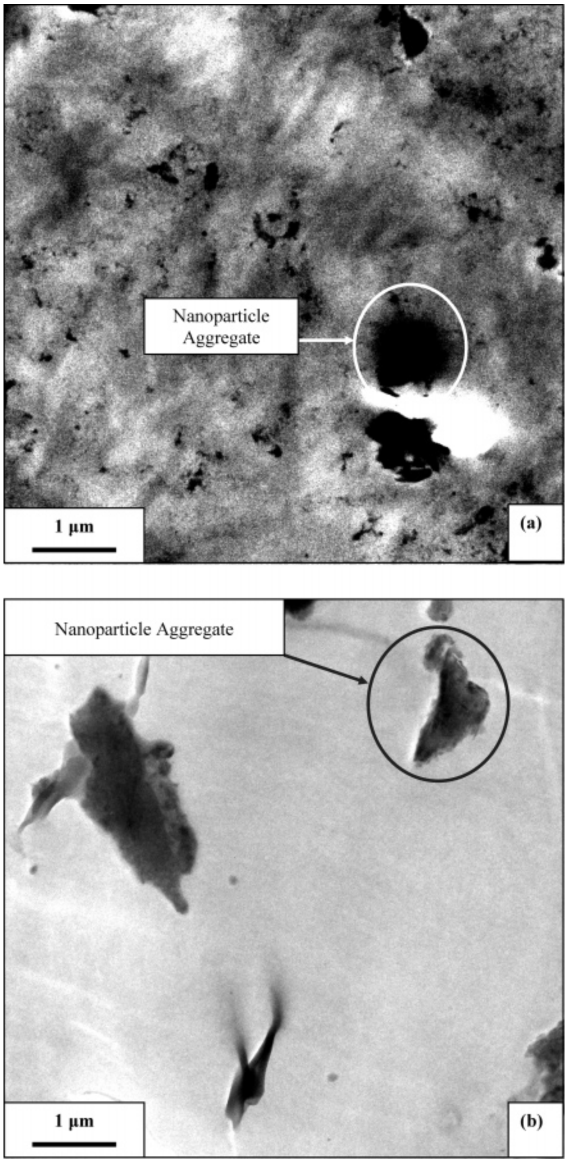

Figure 6. TEM images of (a) PB containing 10 vol % (nominal) MgO and (b) PB containing 20 vol % (nominal) MgO.

(i.e., polymer or voids). Figure 6a shows numerous well-dispersed nanoparticle aggregates with characteristic dimensions in the submicron and micron range.

The nanoparticle aggregates in the sample containing 20 vol % (nominal) MgO are larger and less uniformly dispersed than those in the film containing 10 vol % (nominal) MgO. The larger aggregate size in the more highly concentrated sample may be due, in part, to more incomplete mixing in the sample containing a higher concentration of particles, since sample viscosity increased with increasing particle concentration. The presence of large aggregates of particles could, in turn, promote the formation of large nanoparticle aggregates at the expense of smaller aggregates or individually dispersed particles.[55]

Nanocomposite Density and Void Volume. Based on the density data presented below, the inclusion of nanoparticles in PB results in the formation of voids in the sample. This point is readily apparent if one compares the experimentally determined density of the nanocomposite samples to the so-called additive density, ρ_{Add}, which is the density that a nanocomposite sample would have if the polymer and particles each exhibited their pure component properties:[12]

$$\rho_{\mathrm{Add}} = \phi_{\mathrm{F}}^{\mathrm{N}} \rho F + (1 - \phi_{\mathrm{F}}^{\mathrm{N}})(\phi_{\mathrm{C}} \rho_{\mathrm{C}} + (1 - \phi_{\mathrm{C}}) \rho_{\mathrm{A}}) \quad (24)$$

where ϕ_{C} is the crystalline phase volume percent from WAXD (cf. Table 1) and ρ_{F} is the pure filler density. Figure 7 presents the experimentally determined density, ρ_{Exp}, as a function of particle content in the sample. As nanoparticle concentration increases, the experimental density deviates more and more from the additive model given by eq 24.

The departure of ρ_{Exp} from ρ_{Add} can be characterized in terms of the "void" volume fraction, ϕ_{V}, in the sample:[11]

$$\phi_{\mathrm{V}} = 1 - \frac{\rho_{\mathrm{Exp}}}{\rho_{\mathrm{Add}}} \quad (25)$$

Using the data in Figure 7, the void volume was calculated and is presented as a function of particle loading in Figure 8. At loadings of ~25 vol % (nominal) MgO, the void volume percent is ~52%, so most of the sample is voids at the highest loadings considered. Other nanocomposite systems also exhibit an increase in void volume fraction with increasing particle loading, and various groups have assigned the voids to the polymer−particle interface,[56] polymer free volume,[49] or interparticle spaces.[47] On the basis of the information available, we cannot definitively assign the voids in MgO filled PB nanocomposites to any one or combination of these locations. However, it is quite clear that including these very small particles in the polymer results in strong deviations away from the additive density model presented above.

Given the non-negligible volume of voids in the nanocomposites, the true and nominal volume fraction of MgO are not the same. The true volume fraction of MgO in the PB matrix, $\phi_{\mathrm{F}}^{\mathrm{T}}$, may be calculated as follows:[11]

$$\phi_{\mathrm{F}}^{\mathrm{T}} = \phi_{\mathrm{F}}^{\mathrm{N}}(1 - \phi_{\mathrm{V}}) \quad (26)$$

The maximum difference $\phi_{\mathrm{F}}^{\mathrm{N}}$ between and $\phi_{\mathrm{F}}^{\mathrm{T}}$ occurs at the maximum particle loadings, where $\phi_{\mathrm{F}}^{\mathrm{N}}$ is 27% and $\phi_{\mathrm{F}}^{\mathrm{T}}$ is 13%, according to eq 26 and the data in Figures 7 and 8.

Gas Permeability. In MgO-filled PB films, CO_2, N_2, and CH_4 permeability increases with increasing particle loading, as presented in Figure 9. The CO_2, CH_4, and N_2 permeability values are approximately 10, 17, and 18 times higher, respectively, in PB containing 27 vol % (nominal) MgO than in unfilled PB. Gas permeability values are considerably higher for the nanocomposite samples than predicted by eq 7 for heterogeneous films with an impermeable discontinuous phase.

In previous studies involving dispersion of nanoparticles in PB, the increase in gas permeability with increasing particle loading could be rationalized using Bruggeman's model if the model were applied in the limit where the dispersed phase was much more permeable than the matrix (i.e., eq 6), and the dispersed phase volume fraction was set equal to the volume fraction of voids in the sample.[12] This approach was applied to the data from the present study. The results are presented in Figure 10, which shows the correlation between relative CO_2, CH_4, and N_2 permeability (i.e., permeability in a composite sample relative to that of unfilled PB) and void volume. The dashed line represents eq 6 when the dispersed phase volume fraction is set equal to the void volume fraction (i.e., $\phi_{\mathrm{D}} = \phi_{\mathrm{V}}$). Interestingly, eq 6 captures the observed trend in permeability at low void volumes but does not increase as strongly with void volume as the void volume percent increases beyond ~10%.

The strong increase in permeability values at high particle loadings could suggest that the particles were introducing

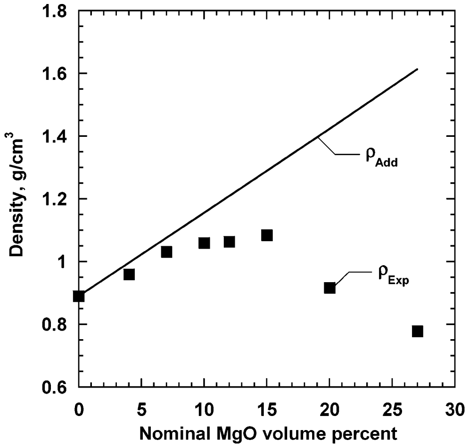

Figure 7. Effect of MgO concentration on composite density (ρ_{Exp}, ■). The solid line represents the additive density, ρ_{Add}, calculated according to eq 24.

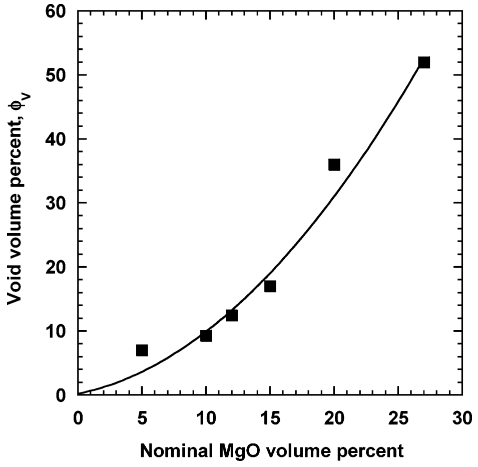

Figure 8. Void volume percent of PB/MgO nanocomposite films as calculated from the data in Figure 7 using eq 25. The solid line is drawn to guide the eye.

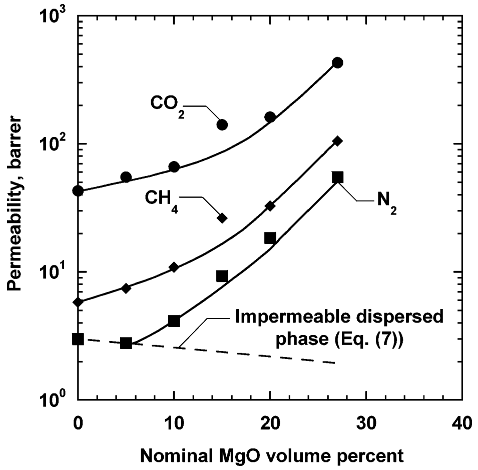

Figure 9. Effect of MgO concentration on CO_2 (●), CH_4 (◆), and N_2 (■) permeability at $\Delta p = 6$ atm. Measurements were conducted at 35 °C and at a downstream pressure less than 0.01 atm. The dashed line represents Bruggeman's model for N_2 in the limit where the nanoparticles are treated as an impermeable dispersed phase (i.e., eq 7) present at levels corresponding to the nominal volume fraction loading of particles in the polymer. The solid lines are drawn to guide the eye.

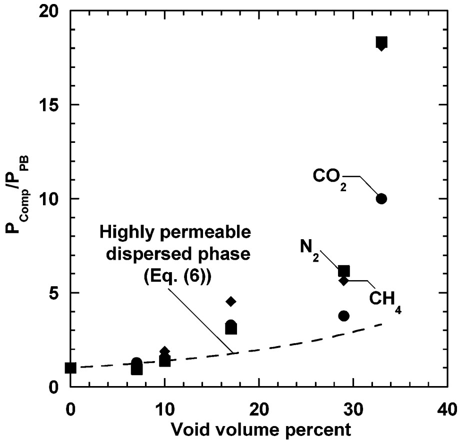

Figure 10. Permeability of nanocomposite samples, P_{Comp}, relative to the permeability of nitrogen in 1,2-polybutadiene, P_{PB} for CO_2 (●), CH_4 (◆), and N_2 (■). The dashed line represents Bruggeman's model in the limit where the dispersed phase is highly permeable (i.e., eq 6). The volume fraction of the dispersed phase in this model was set equal to the void volume estimated from the density data (i.e., eq 25). The experimental permeability data were collected at 35 °C and $\Delta p = 6$ atm.

transmembrane defects.[57] In this case, the gas transport properties would be expected to be more similar to the properties observed with either Knudsen diffusion or Poiseuille flow.[10] In the case of Poiseuille flow, gas permeability would be pressure dependent.[11] Figure 11 presents the influence of upstream pressure on gas permeability for PB and PB-filled MgO. Permeability values for the unfilled polymer are similar to the values from Naito et al., who reported CO_2, CH_4, and N_2 permeability coefficients of 43, 5.6, and 1.9 barrer, respectively, in PB.[58] Although CO_2 permeability does increase with pressure, this behavior may be attributed to CO_2-induced plasticization.[12] Both CH_4 and N_2 permeabilities are independent of pressure, which suggests that gas transport in the nanocomposite does not follow Poiseuille flow.

The gas selectivities expected in films containing transmembrane defects could be either the Knudsen, $\alpha^{K}_{A/B}$, or Poiseuille limit, $\alpha^{P}_{A/B}$. The Knudsen limit is[59]

$$\alpha^{K}_{A/B} = \sqrt{\frac{M_B}{M_A}} \tag{27}$$

where M_A and M_B are the molar masses of gases A and B, respectively.[60] The Poiseuille selectivity limit for gases tested individually is[60]

$$\alpha^{P}_{A/B} = \frac{\mu_B}{\mu_A} \tag{28}$$

where μ_A and μ_B are the viscosities of gas A and B, respectively.[60] However, if gases are tested in mixtures and undergo Poiseuille flow, then the observed selectivity would be 1. Figure 12 presents pure gas selectivity values for the gas pairs considered as a function of increasing particle loading. Table 3 presents a comparison of the pure gas selectivity values in unfilled PB, PB filled with the highest content of particles considered (27 vol % (nominal)), and the Knudsen and Poiseuille limits, calculated based on eqs 27 and 28. In the case of CO_2/N_2 and CO_2/CH_4, selectivity decreases with increasing particle loading but never reaches values that are consistent with either Poiseuille or Knudsen flow, suggesting that the films are free from macroscopic, trans-film defects. The CH_4/N_2 selectivity did not deviate significantly from 2 (i.e., the unfilled polymer CH_4/N_2 selectivity) with increasing particle concentration, indicating that methane and nitrogen permeability exhibited essentially the same relative dependence on particle content.

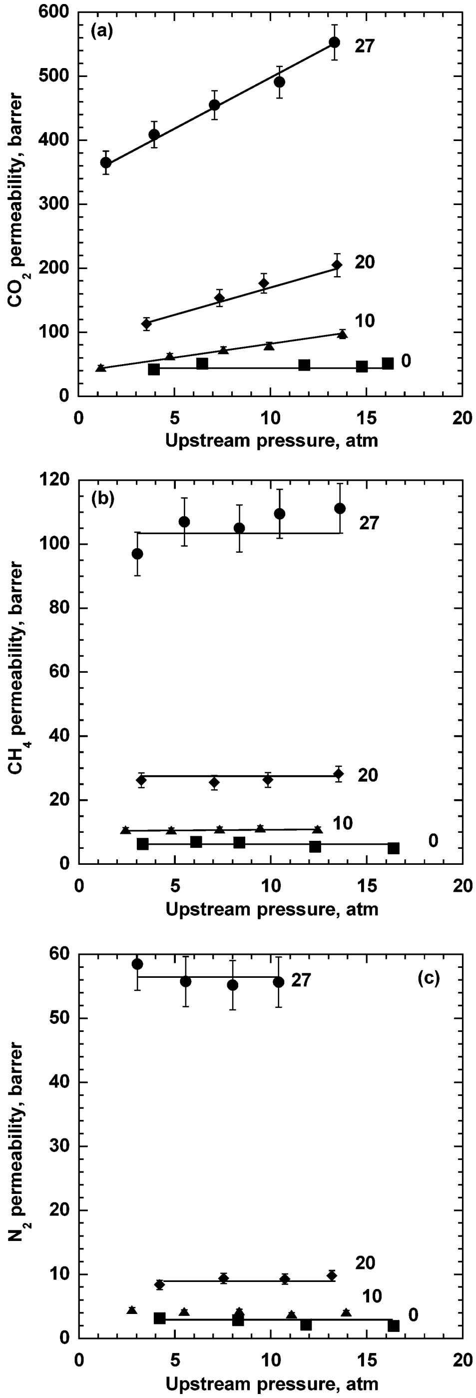

Figure 11. Effect of upstream pressure on pure gas (a) CO_2, (b) CH_4, and (c) N_2 permeability of PB containing various amounts of MgO. The numbers next to the data represent the nominal volume percent of MgO in the sample. These measurements were conducted at 35 °C and at atmospheric downstream pressure. The solid lines are provided to guide the eye. Uncertainties are estimated using the propagation of errors method.[25]

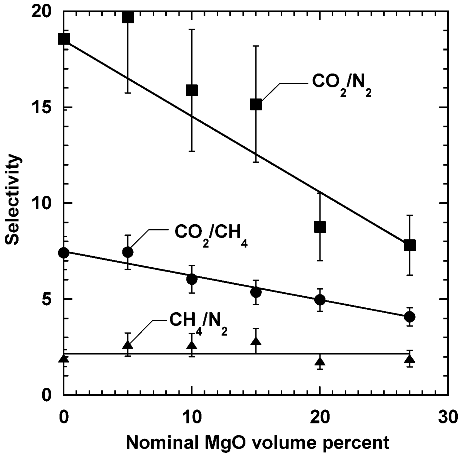

Figure 12. Effect of MgO concentration on pure gas CO_2/N_2 (■), CO_2/CH_4 (●), and CH_4/N_2 (▲) selectivity at $\Delta p = 6$ atm. Measurements were made at 35 °C and a downstream pressure less that 0.01 atm. The trend lines are drawn to guide the eye. Uncertainties are estimated using the propagation of errors method.[25]

Table 3. Comparison of Pure Gas Selectivity Values in Unfilled and Filled 1,2-Polybutadiene with Values Expected for Knudsen and Poiseuille Flow at 35 °C

gas pair	Knudsen selectivity	Poiseuille selectivity	unfilled PB	PB filled with 27 vol % (nominal) MgO
CO_2/N_2	0.8	1.2	14	7.8
CO_2/CH_4	0.6	0.7	7.4	4.1
CH_4/N_2	1.3	0.6	1.9	1.9

Based on the lack of pressure dependence for CH_4 and N_2 permeabilities and the strong deviations between the selectivity values observed in the nanoparticle-filled samples and the selectivity values expected for flow through pores, the presence of MgO nanoparticles increases permeability without introducing trans-film defects in amounts sufficient to drive selectivity to values consistent with pore flow models, such as Knudsen flow.

Gas Solubility. The Freundlich isotherm is an empirical model used to characterize the effect of pressure on the amount of gas adsorbed on mineral surfaces, C_f:[61]

$$C_f = Kp^{1/n} \tag{29}$$

where K and n are temperature-dependent fitting parameters[61] and p is the gas pressure. In contrast to models such as the Langmuir isotherm, the Freundlich isotherm does not limit the amount of gas adsorbed as pressure increases.[61] Equation 29 has been used to model gas adsorption on TiO_2 nanoparticles in polymer-based nanocomposites.[11,61,62] The concentration of light gases in rubbery polymers usually obeys Henry's law:[5]

$$C = k_D p \tag{30}$$

where k_D is the Henry's law constant and p is the gas pressure. The CO_2, CH_4, and N_2 Freundlich equation parameters for adsorption on MgO nanoparticles and the Henry's law parameters for sorption in unfilled PB are presented in Table 4.[62,63] The Henry's law values listed in Table 4 are consistent with those reported in the literature.[58]

Gas sorption in polymer crystals is typically negligible.[64] Therefore, the Henry's law parameter for the amorphous polymer phase in a nanocomposite, $k_{D,A}$, can be estimated as follows:[65]

$$k_{D,A} = \frac{k_D}{1 - \phi_{C,0}} \tag{31}$$

where $\phi_{C,0}$ (cm^3 crystals/cm^3 polymer) is the crystalline polymer volume fraction of the pure (i.e., unfilled) polymer.

The adsorption isotherms for CO_2, CH_4, and N_2 at 35 °C on MgO nanoparticles are presented in Figure 13. For comparison, the CO_2 sorption isotherm in unfilled PB is also included in this figure. The amount of gas sorbed per unit volume of particles is orders of magnitude higher than the amount of gas sorbed per unit volume of polymer. To put these sorption values in perspective, Table 5 presents the amounts of various gases sorbed onto the particles and in the polymer. In some cases,

Table 4. Freundlich Isotherm Parameters for Adsorption onto MgO and Henry's Law Sorption Parameters for 1,2-Polybutadiene[a]

penetrant	K (cm^3 (STP))/ (cm^3 MgO atm$^{1/n}$)	n	k_D (cm^3 (STP))/(cm^3 PB atm) (Matteucci et al.)	k_D (cm^3 (STP))/(cm^3 PB atm) (Naito et al.)
N_2	31 ± 7	2.6 ± 0.2	0.03 ± 0.01	0.04
CH_4	50 ± 8	2.5 ± 0.2	0.21 ± 0.01	0.23
CO_2	63 ± 10	3.4 ± 0.2	0.71 ± 0.06	0.81

[a] Freundlich isotherm parameters were obtained from experimental results at 35 °C. Uncertainties were estimated using the least-squares fit method.[25] Matteucci et al. reported Henry's law parameters for light gases in 1,2-polybutadiene at 35 °C,[12] while the values reported by Naito et al. were determined at 25 °C.[58]

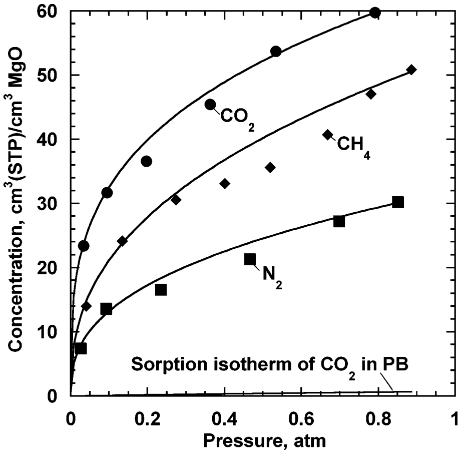

Figure 13. Pure gas CO_2 (●), CH_4 (◆), and N_2 (■) adsorption isotherms on MgO and CO_2 sorption isotherm in PB at 35 °C.[16] The CO_2 sorption isotherm was estimated by eq 30 using the Henry's law parameters from Matteucci et al.[16] listed in Table 5. The lines are drawn to assist the reader.

Table 5. CO_2, CH_4, and N_2 Concentration on MgO Nanoparticles and PB at 35 °C and 0.9 atm[a]

penetrant	C_f (cm^3 (STP))/(cm^3 MgO)	C (cm^3 (STP))/(cm^{3}PB)
N_2	30 ± 4	0.03 ± 0.01
CH_4	48 ± 5	0.18 ± 0.01
CO_2	67 ± 7	0.63 ± 0.06

[a] Uncertainties were estimated using the propagation of errors method.[25]

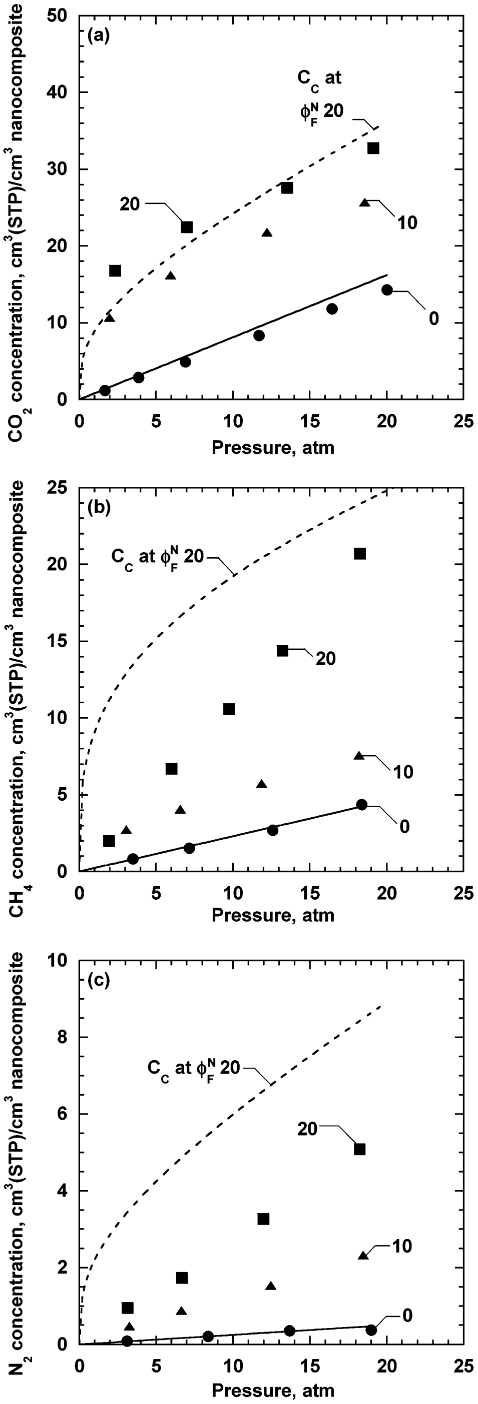

Figure 14. Sorption isotherms for (a) CO_2, (b) CH_4, and (c) N_2 in PB (●) and PB containing 10 (▲) and 20 (■) vol % (nominal) MgO. The temperature was 35 °C. The dashed line represents the gas uptake according to the additive sorption model (i.e., eq 32). The solid line represents gas concentration in PB at 25 °C according to eq 30 using the k_D values from Naito et al.[58]

the particles sorb more than 2 orders of magnitude more gas per unit volume than the polymer.

Figure 14 presents the sorption isotherms for CO_2, CH_4, and N_2 in PB and nanocomposites containing various concentrations of MgO. Gas sorption in the nanocomposites was consistently higher than in unfilled PB, as might be expected since the particles inherently sorb much more gas per unit volume than the polymer. If the concentration of gas sorbed by the particles, polymer, and voids in the nanocomposite sample were equal to their pure component values (i.e., if the observed nanocomposite sorption were the additive sum of the contributions of each of the constituent components, weighted according to their concentration), then the gas concentration in the composite, C_C, would be given by[11]

$$C_C = (\phi_F^N K p^{1/n} + (1-\phi_F^N)(1-\phi_C)k_{D,A}p)(1-\phi_V) + \frac{p\phi_V}{RT} \qquad (32)$$

The final term in eq 32 accounts for the gas concentration in the void space according to the ideal gas law.[60] Based on calculations using the parameters in Table 4 and the void volume values from Figure 8, the sorption of gas on the nanoparticle surface dominates overall nanocomposite sorption in eq 32. For example, at 1 atm, eq 32 predicts that the adsorption of CO_2 on the nanoparticle surface would account for ∼78% of the gas sorbed into a nanocomposite containing 5 vol % (nominal) MgO and 5 vol % voids.

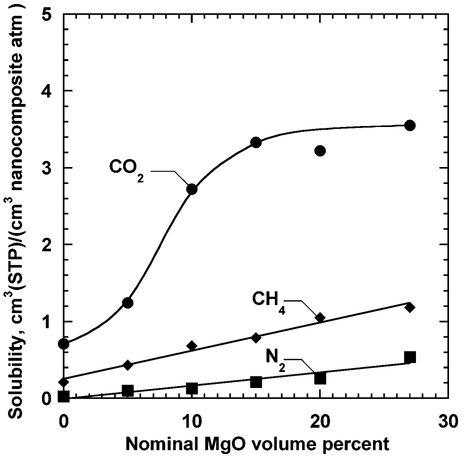

Figure 15. Effect of MgO concentration on CO_2 (●), CH_4 (◆), and N_2 (■) solubility at 6 atm and 35 °C. Solubility values were estimated using eq 3, and concentration values were linearly interpolated to 6 atm. Trend lines are drawn to guide the eye.

Qualitatively, the gas uptake increases with increasing particle content, consistent with the trend anticipated by eq 32. Quantitatively, the agreement between the model and CO_2 is fairly good, particularly considering that the particle sorption data used to determine the Freundlich isotherm parameters was obtained up to ~1 atm, and the data in Figure 14 extend to ~20 atm. However, eq 32 overestimates the CH_4 and N_2 concentration in the nanocomposites. In previous studies of nanocomposite sorption, it was not unusual to observe sorption levels in the nanocomposites that were lower than expected on the basis of simple additive models.[12,16,22] This effect has been related to the fact that, in many cases, polymers are known to interact with particles and can readily adsorb on particle surfaces.[66] The absorbed polymer chains occupy sorption sites on the particle surface that could otherwise adsorb gas.[22] This mechanism could certainly be supposed to be active in the present study. However, it is not clear why eq 32 provides a better estimate of CO_2 uptake than it does of the nonpolar gases.

The presence of nanoparticles in PB substantially increases CO_2, CH_4, and N_2 solubility. Figure 15 presents gas solubility in PB as a function of MgO particle concentration. Solubility was estimated by linearly interpolating the concentration data (cf. Figure 14) to 6 atm and applying eq 3. The CO_2 solubility is 3.6 $cm^3/(cm^3$ (nanocomposite) atm) in films containing 27 vol % (nominal) MgO, which is 5.1 times the CO_2 solubility in unfilled PB at 6 atm and 35 °C. In films containing 27 vol % (nominal) MgO, CH_4 solubility is 1.2 $cm^3/(cm^3$ (nanocomposite) atm) at 6 atm and 35 °C, which is 6 times the solubility of CH_4 in unfilled PB (i.e., 0.21 cm^3 (STP)/(cm^3 atm)). The N_2 solubility in PB films containing 27 vol % (nominal) MgO was 0.54 $cm^3/(cm^3$ nanocomposite atm) at 6 atm and 35 °C, which is 21 times higher than the N_2 solubility in unfilled PB. The increase in solubility is due mainly to adsorption of gas by the particles. Based on the values in Table 5, the particles (at the conditions presented in Table 5) sorb approximately 100, 270, and 1000 times more CO_2, CH_4, and N_2 than unfilled PB, respectively.

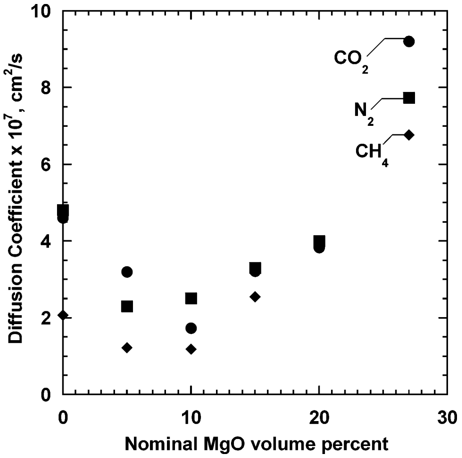

Figure 16. Effect of MgO concentration on CO_2 (●), CH_4 (◆), and N_2 (■) diffusion coefficients at $\Delta p = 6$ atm, calculated according to eq 2. Permeability values used in this calculation are from experimental data at 35 °C and $\Delta p = 6$ atm, and the solubility coefficients are reported in Figure 15.

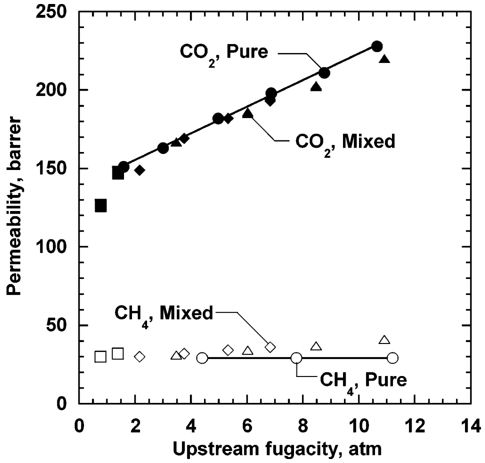

Figure 17. CO_2 (●) and CH_4 (○) pure gas permeability coefficients and CO_2 and CH_4 mixed gas permeability coefficients in 1,2-polybutadiene containing 20 vol % (nominal) MgO at 35 °C. The fugacity was varied by varying total feed pressure and by using gas mixtures of the following compositions: 20/80 (■, □), 50/50 (◆, ◇), and 80/20 (▲, △) (mol/mol) CO_2/CH_4. CO_2 and CH_4 permeability coefficients are represented by the filled and unfilled symbols, respectively. For the pure gas permeability data, the fugacity axis is the pure gas fugacity. The mixture permeation data for both CO_2 and CH_4 are plotted as a function of CO_2 fugacity in the feed gas mixture. Trend lines are drawn to assist the reader.

Figure 16 presents diffusion coefficients calculated using eq 2, using permeability coefficients from experimental data at 35 °C and $\Delta p = 6$ atm and solubility values from Figure 15. Gas diffusion coefficients initially decrease with increasing particle loading, which may be attributed to the presence of impermeable particles, which would increase the tortuosity of the diffusion pathway a penetrant gas would take to cross the film, and to a reduction in bulk polymer chain mobility, as indicated by the increase in T_g as shown in Table 1. At particle loadings above 10 vol % (nominal) MgO, the gas diffusion coefficients increased with increasing particle concentration. The creation of void space within the composite could contribute to increases in diffusion coefficients with increasing particle content, which corresponds to increasing levels of voids in the samples.

Mixed Gas Transport. Often pure gas permeability values are not the same as the permeability of the same gas measured in gas mixtures, particularly if at least one of component is a strongly swelling penetrant such as CO_2.[5,67] The CO_2/CH_4 mixed gas permeability behavior of PB containing 20 vol % (nominal) MgO is presented in Figure 17. Fugacity is used to report these results to account for the nonideal behavior of the gas mixtures. Fugacity was calculated using the Soave−Redlich−Kwong (SRK) equation.[44,68,69]

As indicated in Figure 17, the permeability of both CO_2 and CH_4 increases with increasing CO_2 fugacity. For example, the CH_4 permeability increases from 30 to 41 barrer as CO_2 fugacity

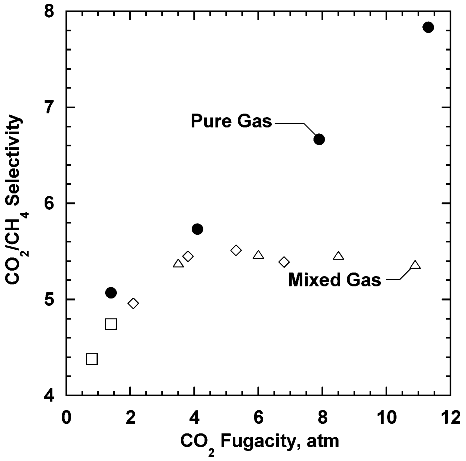

Figure 18. Effect of upstream CO_2 fugacity on pure and (●) mixed gas CO_2/CH_4 selectivity in 1,2-polybutadiene containing 20 vol % (nominal) MgO at 35 °C. The CO_2 fugacity was varied by varying total feed pressure and by using gas mixtures of the following compositions: 20/80 (□), 50/50 (◇), and 80/20 (△) (mol/mol) CO_2/CH_4. The mixture selectivity data are plotted as a function of CO_2 fugacity in the feed gas mixture. The pure gas selectivity value at 1.4 atm is calculated from the pure gas CH_4 permeability value at 4.1 atm, since pure gas CH_4 permeability is pressure independent.

increases from 1.6 to 12 atm. Such behavior is often ascribed to plasticization, and it generally occurs when one or more of the penetrant gases is present at sufficiently high concentrations within the polymer matrix to increase polymer chain mobility.[70−72] The pure gas nanocomposite CO_2 permeability also increases with increasing CO_2 fugacity, suggesting that the increase in CH_4 permeability with increasing CO_2 fugacity in the mixture is due to the presence of CO_2.

Figure 18 presents pure and mixed gas CO_2/CH_4 selectivity as a function of upstream CO_2 fugacity. In the pure gas case, selectivity increases with increasing CO_2 fugacity since CO_2 permeability increases with increasing CO_2 fugacity. In the mixed gas case, the selectivity is lower than the pure gas case. Moreover, the selectivity increases with increasing CO_2 fugacity up to about 4 atm, primarily because CH_4 permeability is approximately constant over this range of CO_2 fugacity values, but CO_2 permeability increases steadily, as shown in Figure 17. At higher CO_2 fugacity values, the mixed gas selectivity reaches a maximum and decreases slightly with increasing CO_2 fugacity. This result occurs because CH_4 permeability begins to increase with increasing CO_2 fugacity, suggesting the onset of CO_2-induced plasticization at CO_2 fugacities beyond about 4 atm. The increase in selectivity with increasing CO_2 fugacity at low CO_2 fugacity values may be due to more favorable adsorption of CO_2 on the particles in the gas mixture (i.e., an increase in the CO_2/CH_4 solubility selectivity) as CO_2 fugacity increases, though this hypothesis is speculative at this time and has not been proven.

Conclusions

MgO-filled PB nanocomposites exhibited higher permeability than the unfilled polymer. As particle loading increased, nanocomposite density deviated from the additive density model, which indicated that voids were present in the nanocomposite films. As the void concentration increased, gas permeability increased. The increase in permeability was partially due to increases in gas solubility coefficients that occurred as MgO concentration in the nanocomposites increased. Diffusion coefficients were lower than in the unfilled polymer at low particle loading but increased at higher loadings to levels that were higher than the unfilled polymer at the highest particle loadings considered. For instance, in a PB film containing 27 vol % (nominal) MgO, about 60% of the CH_4 permeability increase, relatively to an unfilled sample, can be attributed to an increase in solubility, while the remaining 40% of the increase can be attributed to an increase in the methane diffusion coefficient.

Acknowledgment. We gratefully acknowledge partial support of this work by the U.S. Department of Energy (Grant DE-FG02-02ER15362), the National Science Foundation (CTS-0515425), and the Welch Foundation. The authors also warmly acknowledge Steve Werner and Dr. Jing Li of the Dow Chemical Company for sharing their expertise regarding AFM sample preparation and experimental procedure.

References and Notes

(1) Baker, R. W. Future directions of membrane gas separation technology. *Ind. Eng. Chem. Res.* **2002**, *41*, 1393−1411.

(2) Powell, C. E.; Qiao, G. G. Polymeric CO_2/N_2 gas separation membranes for the capture of carbon dioxide from power plant flue gases. *J. Membr. Sci.* **2006**, *279*, 1−49.

(3) Freeman, B. D. Basis of permeability/selectivity tradeoff relations in polymeric gas separation membranes. *Macromolecules* **1999**, *32*, 375−380.

(4) Robeson, L. M. Correlation of separation factor versus permeability for polymeric membranes. *J. Membr. Sci.* **1991**, *62*, 165−185.

(5) Matteucci, S.; Yampol'skii, Y. P.; Freeman, B. D.; Pinnau, I. Transport of gases and vapors in glassy and rubbery polymers. In *Materials Science of Membranes for Gas and Vapor Separations*; Yampol'skii, Y. P., Freeman, B. D., Pinnau, I., Eds.; John Wiley and Sons: London, 2006; pp 1−48.

(6) Park, H. B.; Jung, C. H.; Lee, Y. M.; Hill, A. J.; Pas, S. J.; Mudie, S. T.; van Wagner, E.; Freeman, B. D.; Cookson, D. J. Polymers with cavities tuned for fast selective transport of small molecules and ions. *Science* **2007**, *318*, 254−258.

(7) Vu, D. Q.; Koros, W. J.; Miller, S. J. Mixed, matrix membranes using carbon molecular sieves I. Preparation and experimental results. *J. Membr. Sci.* **2003**, *211*, 311−334.

(8) He, Z.; Pinnau, I.; Morisato, A. Nanostructured poly(4-methyl-2-pentyne)/silica hybrid membranes for gas separation. *Desalination* **2002**, *146*, 11−15.

(9) Merkel, T. C.; Freeman, B. D.; Spontak, R. J.; He, Z.; Pinnau, I.; Meakin, P.; Hill, A. J. Ultrapermeable, reverse-selective nanocomposite membranes. *Science* **2002**, *296*, 519−522.

(10) Merkel, T. C.; He, Z.; Pinnau, I.; Freeman, B. D.; Hill, A. J.; Meakin, P. Effect of nanoparticles on gas sorption and transport in poly(1-trimethylsilyl-1-propyne). *Macromolecules* **2003**, *36*, 6844−6855.

(11) Matteucci, S.; Kusuma, V. A.; Sanders, D.; Swinnea, S.; Freeman, B. D. Gas transport in TiO_2 nanoparticle filled poly(1-trimethylsilyl-1-propyne). *J. Membr. Sci.* **2008**, *307*, 196−217.

(12) Matteucci, S.; Kusuma, V. A.; Swinnea, S.; Freeman, B. D. Light gas permeability, solubility and diffusion in 1,2-polybutadiene containing brookite nanoparticles. *Polymer*, **2008**, *49*, 757−773.

(13) Barsema, J. N.; Balster, J.; Jordan, V.; van der Vegt, N. F. A.; Wessling, M. Functionalized carbon molecular sieve membranes containing Ag-nanoclusters. *J. Membr. Sci.* **2003**, *219*, 47−57.

(14) Kang, Y. S.; Kang, S. W.; Kim, H.; Kim, J. H.; Won, J.; Kim, C. K.; Char, K. Interaction with olefins of the partially polarized surface of silver nanoparticles activated by *p*-benzoquinone and its implications for facilitated olefin transport. *Adv. Mater.* **2007**, *19*, 475−479.

(15) Paul, D. R.; Kemp, D. R. Diffusion Time Lag in Polymer Membranes Containing Adsorptive Fillers. *J. Polym. Sci., Polym. Symp.* **1973**, *41*, 79−93.

(16) Matteucci, S.; Kusuma, V. A.; Kelman, S.; Freeman, B. D. Gas transport properties in MgO nanoparticle filled poly(1-trimethylsilyl-1-propyne), *Polymer*, in press.

(17) Mekhemer, G. A. H.; Halaway, S. A.; Mohamed, M. A.; Zaki, M. I. Qualitative and quantitative assessments of acid and base sites exposed on polycrystalline MgO surfaces: Thermogravimetric, calorimetric, and in-situ FTIR spectroscopy study combination. *J. Phys. Chem. B* **2004**, *108*, 13379−13386.

(18) Stark, J. V.; Park, D. G.; Lagadic, I.; Klabunde, K. J. Nanoscale, metal oxide particles/clusters as chemical reagents. Unique surface chemistry on magnesium oxide as shown by enhanced adsorption of acid gases (sulfur dioxide and carbon dioxide) and pressure dependence. *Chem. Mater.* **1996**, *8*, 1904−1912.

(19) Ghosal, K.; Freeman, B. D. Gas separation using polymer membranes: An overview. *Polym. Adv. Technol.* **1994**, *5*, 673−697.

(20) Bouma, R. H. B.; Checchetti, A.; Chidichimo, G.; Drioli, E. Permeation through a heterogeneous membrane: The effect of the dispersed phase. *J. Membr. Sci.* **1997**, *128*, 141−149.

(21) Vu, D. Q.; Koros, W. J.; Miller, S. J. Mixed matrix membranes using carbon molecular sieves II. Modeling permeation behavior. *J. Membr. Sci.* **2003**, *211*, 335−348.

(22) Barrer, R. M.; Barrie, J. A.; Rogers, M. G. Heterogeneous membranes: Diffusion in filled rubber *J. Polym. Sci., Part A: Polym. Chem.* **1963**, *1*, 2565−2586.

(23) Utamapanya, S.; Klabunde, K. J.; Schlup, J. R. Nanoscale metal oxide particles/clusters as chemical reagents. Synthesis and properties of ultrahigh surface area magnesium hydroxide and magnesium oxide. *Chem. Mater.* **1991**, *3*, 175−181.

(24) Obata, Y.; Tosaki, C.; Ikeyama, M. Bulk properties of syndiotactic 1,2-polybutadiene. I. Thermal and viscoelastic properties. *Polym. J.* **1975**, *7*, 207−216.

(25) Bevington, P. R.; Robinson, D. K. *Data Reduction and Error Analysis for the Physical Sciences*, 3rd ed.; McGraw-Hill: New York, 2003.

(26) Weibull, W. A statistical distribution function of wide applicability. *J. Appl. Mech.* **1951**, *18*, 293−297.

(27) Olkin, I.; Gleser, L. J.; Derman, C. *Probability Models and Applications*, 2nd ed.; Macmillan College Publishing Co.: New York, 1980.

(28) Bryant, G.; Martin, S.; Budi, A.; van Megen, W. Accurate measurement of small polydispersities in colloidal suspensions. *Langmuir* **2003**, *19*, 616−621.

(29) Lin, H.; Freeman, B. D. Gas solubility diffusivity and permeability in poly(ethylene oxide). *J. Membr. Sci.* **2004**, *239*, 105−117.

(30) Natta, G.; Corradini, P. The structure of crystalline 1,2-polybutadiene and of other “syndiotactic polymers”. *J. Polym. Sci.* **1956**, *20*, 251−266.

(31) Matteucci, S.; van Wagner, E.; Swinnea, S.; Freeman, B. D.; Sakaguchi, T.; Masuda, T. Desilylation of substituted polyacetylenes in the presence of nanoparticles. *Macromolecules* **2007**, *40*, 3337−3347.

(32) Natta, G. Determination of the polypropylene crystallinity. *Atti Accad. Naz. Lincei, Rend., Cl. Sci. Fis., Mat. Nat.* **1957**, *22*, 11−17.

(33) Peterson, D. R. The determination of crystallinity in polymers, The Dow Chemical Company, Research Report SL 87902, 1957.

(34) Dhoot, S. N.; Freeman, B. D.; Stewart, M.; Hill, A. J. Sorption and transport of linear alkane hydrocarbons in biaxially oriented poly(ethylene terephthalate). *J. Polym. Sci., Part B: Polym. Phys.* **2001**, *39*, 1160−1172.

(35) Iraqi, A.; Cole-Hamilton, D. J. Preparation and reactivity of polyepoxides and polyketones: Catalytic oxidation of polybutadienes. *J. Mater. Chem.* **1992**, *2*, 183−190.

(36) Ajjou, A. N.; Alper, H. Catalitic oxidation of polybutadienes based on a Wicker-type reaction. *Macromolecules* **1996**, *29*, 5072−5074.

(37) Yin, D.; Zhang, Y.; Pend, Z.; ZHang, Y. Effect of fillers and additives on the properties of SBR vulcanizates. *J. Appl. Polym. Sci.* **2003**, *88*, 775−782.

(38) Westlinning, H.; Fleischhauer, H. *Properties of White Reinforcing FIllers in Elastomers*, In *Reinforcement of Elastomers*; Kraus, G., Ed.; John Wiley and Sons: New York, 1965; pp 425−490.

(39) Wiederhorn, S.; Fields, R.; Low, S.; Bahng, G.; Wehrstedt, A.; Hahn, J.; Tomota, Y.; Miyata, T.; Lin, H.; Freeman, B. D.; Aihara, S.; Hagihara, Y.; Tagawa, T. Mechanical Properties. In *Springer-Handbook of Materials Measurement Methods*; Czichos, H., Smith, L. E., Saito, T., Eds.; Springer: Berlin, 2005; pp 283−397.

(40) Bondar, V. I.; Freeman, B. D.; Pinnau, I. Gas sorption and characterization of poly(ether-b-amide) segmented block copolymers. *J. Polym. Sci., Part B: Polym. Phys.* **1999**, *37*, 2463−2475.

(41) Bondar, V.; Freeman, B. D.; Pinnau, I. Gas transport properties of poly(ether-b-amide) segmented block copolymers. *J. Polym. Sci., Part B: Polym. Phys.* **2000**, *38*, 2051−2062.

(42) Stern, S. A.; Gareis, P. J.; Sinclair, T. F.; Mohr, P. H. Performance of a versatile variable-volume permeability cell. Comparison of gas permeability measurements by the variable-volume and variable-pressure methods. *J. Appl. Polym. Sci.* **1963**, *7*, 2035−2051.

(43) O’Brien, K. C.; Koros, W. J.; Barbari, T. A. A new technique for the measurement of multicomponent gas transport through polymeric films. *J. Membr. Sci.* **1986**, *29*, 229−238.

(44) Raharjo, R. D.; Lin, H.; Sanders, D. F.; Freeman, B. D.; Kalakkunnath, S.; Kalika, D. S. Relation between network structure and gas transport in crosslinked poly(propylene glycol diacrylate). *J. Membr. Sci.* **2006**, *283*, 253−265.

(45) Rittigstein, P.; Torkelson, J. M. Polymer-nanocomposite interfacial interactions in polymer nanocomposites: Confinement effects on glass transition temperature and suppression of physical aging. *J. Polym. Sci., Part B: Polym. Phys.* **2006**, *44*, 2935−2943.

(46) Tasagaropoulos, G.; Eisenberg, A. Dynamic mechanical study of the factors affecting the two glass transition behavior of filled polymers. Similarities and differences with random ionomers. *Macromolecules* **1995**, *28*, 6067−6077.

(47) Takahashi, S.; Paul, D. R. Gas permeation in poly(ether imide) nanocomposite membranes based on surface-treated silica. Part 1: Without chemical coupling to matrix. *Polymer* **2006**, *47*, 7519−7534.

(48) Lape, N. K.; Nuxoll, E. E.; Cussler, E. L. Polydisperse flakes in barrier films. *J. Membr. Sci.* **2004**, *236*, 29−37.

(49) Merkel, T. C.; Freeman, B. D.; Spontak, R. J.; He, Z.; Pinnau, I.; Meakin, P.; Hill, A. J. Sorption, transport, and structural evidence for enhanced free volume in poly(4-methyl-2-pentyne)/fumed silica nanocomposite membranes. *Chem. Mater.* **2003**, *15*, 109−123.

(50) Sengupta, R.; Bandyopadhyay, A.; Sabharwal, S.; Chaki, T. K.; Bhomick, A. K. Polyamide-6,6/in situ silica hybrid nanocomposites by sol-gel technique: synthesis, characterization, and properties. *Polymer* **2005**, *46*, 3343−3354.

(51) Ma, D.; Akpalu, Y. A.; Li, Y.; Siegel, R. W.; Schadler, L. S. Effect of titania nanoparticles on the morphology of low density polyethylene. *J. Polym. Sci., Part B: Polym. Phys.* **2005**, *43*, 488−497.

(52) Yang, H.; Bhimaraj, P.; Yang, L.; Siegel, R. W.; Schadler, L. S. Crystal growth in alumina/poly(ethylene terephthalate) nanocomposite films. *J. Polym. Sci., Part B: Polym. Phys.* **2007**, *45*, 747−757.

(53) Mackay, M. E.; Dao, T. T.; Tuteja, A.; Ho, D. L.; Van Horn, B.; Kim, H.-C.; Hawker, C. J. Nanoscale effects leading to non-Eistein-like decrease in viscosity. *Nat. Mater.* **2003**, *2*, 762−766.

(54) Gestoso, P.; Nicol, E.; Doxastakis, M.; Theodorou, D. N. Atomistic Monte Carlo simulation of polybutadiene isomers: *cis*-1,4-polybutadiene and 1,2-polybutadiene. *Macromolecules* **2003**, *36*, 6925−6938.

(55) Osman, M. A.; Atallah, A. interparticle and particle-matrix interactions in polyethylene reinforcement of viscoelasticity. *Polymer* **2005**, *46*, 9476−9488.

(56) Hill, R. J. Diffusive permeability and selectivity of nanocomposite membranes. *Ind. Eng. Chem. Res.* **2006**, *45*, 6890−6898.

(57) Wijmans, J. G.; Baker, R. W. The solution-diffusion model: A unified approach to membrane permeation. In *Materials Science of Membranes for Gas and Vapor Separation*; Yampol’skii, Y. P., Pinnau, I., Freeman, B. D., Eds.; John Wiley & Sons: London, 2006; pp 159−190.

(58) Naito, Y.; Kamiya, Y.; Terada, K.; Mizoguchi, K.; Wang, J.-S. Pressure dependence of gas permeability in a rubbery polymer. *J. Appl. Polym. Sci.* **1996**, *61*, 945−950.

(59) Lindbrathen, A.; Hagg, M.-B. Glass membranes for purification of aggressive gases: Part II. Adsorption measurements and diffusion coefficient estimations. *J. Membr. Sci.* **2005**, *259*, 154−160.

(60) Bird, R. B.; Stewart, W. E.; Lightfoot, E. L. *Transport Phenomena*, 2nd ed.; John Wiley & Sons: New York, 2002.

(61) Do, D. D. *Adsorption Analysis: Equilibria and Kinetics*; Imperial College Press: London, 1998; Vol. 2.

(62) See ref 12.

(63) See ref 16.

(64) Weinkauf, D. H.; Paul, D. R. *Effects of structural order on barrier properties*, In *Barrier Polymers and Structures*; Koros, W. J., Ed.; American Chemical Society: Washington, DC, 1990; pp 60−91.

(65) Michaels, A. S.; Bixler, H. J. Solubility of gases in polyethylene. *J. Polym. Sci.* **1961**, *50*, 393−412.

(66) Kraus, G. Interactions between elastomers and reinforcing fillers. In *Reinforcement of Elastomers*; Kraus, G., Ed.; John Wiley & Sons: New York, 1965; pp 125−152.

(67) Bos, A.; Punt, I. G. M.; Wessling, M.; Strathmann, H. Suppression of CO_2- plasticization by semiinterpenetrating polymer network formation. *J. Polym. Sci., Part B: Polym. Phys.* **1998**, *36*, 1547−1556.

(68) Raharjo, R.; Freeman, B. D.; Paul, D. R.; Sarti, G. C.; Sanders, E. S. Pure and mixed gas CH_4 and n-C_4H_{10} permeability and diffusivity in poly(dimethylsiloxane). *J. Membr. Sci.* **2007**, *292*, 45−61.

(69) Poling, B. E.; Prausnitz, J. M.; O’Connell, J. P. *The Properties of Gases and Liquids*; McGraw-Hill: New York, 2001.

(70) Visser, T.; Koops, G. H.; Wessling, M. On the subtle balance between competitive sorption and plasticization effects in asymmetric hollow fiber gas separation membranes. *J. Membr. Sci.* **2005**, *252*, 265−277.

(71) Staudt-Bickel, C.; Koros, W. J. Improvement of CO_2/CH_4 separation characteristics of polyimides by chemical crosslinking. *J. Membr. Sci.* **1999**, *155*, 145−154.

(72) Koros, W. J.; Hellums, M. W. *Transport Properties*, In *Encyclopedia of Polymer Science and Engineering*, 2nd ed.; John Wiley and Sons: New York, 1989; Suppl. Vol., pp 724−802.

MA702459K